

Reverse Micelle Strategy for the Synthesis of MnOx–TiO2 Active Catalysts for NH3-Selective Catalytic Reduction of NOx at Both Low Temperature and Low Mn Content

*Original*

Reverse Micelle Strategy for the Synthesis of MnOx–TiO2 Active Catalysts for NH3-Selective Catalytic Reduction of NOx at Both Low Temperature and Low Mn Content / Bonelli, Barbara; Tammaro, Olimpia; Martinovic, Ferenc; Nasi, Roberto; Dell'Agli, Gianfranco; Rivolo, Paola; Giorgis, Fabrizio; Ditaranto, Nicoletta; Deorsola, FABIO ALESSANDRO; Esposito, Serena. - In: ACS OMEGA. - ISSN 2470-1343. - ELETTRONICO. - 6:(2021), pp. 24562-24574.  
[10.1021/acsomega.1c03153]

*Availability:*

This version is available at: 11583/2934959 since: 2021-10-29T14:45:58Z

*Publisher:*

American Chemical Society

*Published*

DOI:10.1021/acsomega.1c03153

*Terms of use:*

This article is made available under terms and conditions as specified in the corresponding bibliographic description in the repository

*Publisher copyright*

(Article begins on next page)

# Reverse Micelle Strategy for the Synthesis of $\text{MnO}_x$ – $\text{TiO}_2$ Active Catalysts for $\text{NH}_3$ -Selective Catalytic Reduction of $\text{NO}_x$ at Both Low Temperature and Low Mn Content

Barbara Bonelli, Olimpia Tammaro, Ferenc Martinovic, Roberto Nasi, Gianfranco Dell'Agli, Paola Rivolo, Fabrizio Georgis, Nicoletta Ditaranto, Fabio Alessandro Deorsola, and Serena Esposito\*



Cite This: *ACS Omega* 2021, 6, 24562–24574



Read Online

ACCESS |



Metrics & More

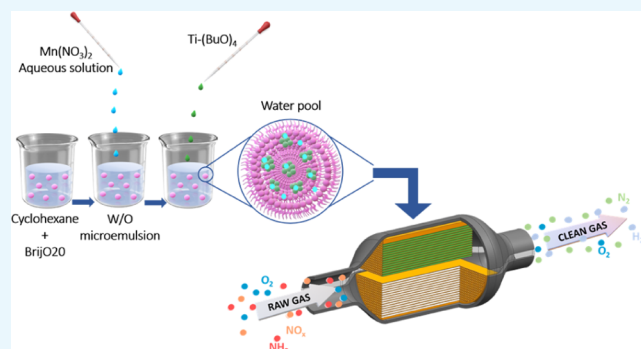


Article Recommendations



Supporting Information

**ABSTRACT:**  $\text{MnO}_x$ – $\text{TiO}_2$  catalysts (0, 1, 5, and 10 wt % Mn nominal content) for  $\text{NH}_3$ -SCR (selective catalytic reduction) of  $\text{NO}_x$  have been synthesized by the reverse micelle-assisted sol–gel procedure, with the aim of improving the dispersion of the active phase, usually poor when obtained by other synthesis methods (e.g., impregnation) and thereby lowering its amount. For comparison, a sample at nominal 10 wt % Mn was obtained by impregnation of the (undoped)  $\text{TiO}_2$  sample. The catalysts were characterized by using an integrated multitechnique approach, encompassing X-ray diffraction followed by Rietveld refinement, micro-Raman spectroscopy,  $\text{N}_2$  isotherm measurement at  $-196^\circ\text{C}$ , energy-dispersive X-ray analysis, diffuse reflectance UV–vis spectroscopy, temperature-programmed reduction technique, and X-ray photoelectron spectroscopy. The obtained results prove that the reverse micelle sol–gel approach allowed for enhancing the catalytic activity, in that the catalysts were active in a broad temperature range at a substantially low Mn loading, as compared to the impregnated catalyst. Particularly, the 5 wt % Mn catalyst showed the best  $\text{NH}_3$ -SCR activity in terms of both  $\text{NO}_x$  conversion (ca. 90%) and the amount of produced  $\text{N}_2\text{O}$  (ca. 50 ppm) in the 200–250  $^\circ\text{C}$  temperature range.



## 1. INTRODUCTION

Nitrogen oxides ( $\text{NO}_x$ ) are still the major air pollutants that are discharged by both combustion engines, as the primary mobile source, and by power plants and nitric acid production plants, as stationary ones.<sup>1,2</sup> To reduce  $\text{NO}_x$  emissions, multiple denitrification ( $\text{deNO}_x$ ) technologies have emerged; among them, the selective catalytic reduction (SCR) with ammonia ( $\text{NH}_3$ -SCR) is one of the most reliable and common methods due to  $\text{NO}_x$  reduction efficiency, durable performance, and reasonable costs.<sup>3–5</sup>

$\text{TiO}_2$ -supported  $\text{V}_2\text{O}_5$  catalysts, promoted by either  $\text{WO}_3$  or  $\text{MoO}_3$ , have been recognized as the most important commercial system in  $\text{NH}_3$ -SCR, in the name of their high activity and resistance to  $\text{SO}_2$  poisoning.<sup>4,6–8</sup> However, the disadvantages of the narrow range of operating temperature (300–400  $^\circ\text{C}$ ) and of the fast and irreversible deactivation above 450  $^\circ\text{C}$  lead to a pressing need for SCR catalysts characterized by both low cost and low  $T$  efficiency.<sup>6–9</sup>

Various transition metal oxides have also been reported to efficiently catalyze SCR reactions at low  $T$ , where the doping metal content reaches up to 30 wt %.<sup>10</sup> Manganese oxides ( $\text{MnO}_x$ ) have shown excellent performance, mostly ascribed to various types of labile oxygen species and Mn oxidation states ( $\text{Mn}^{2+}$ ,  $\text{Mn}^{3+}$ , and  $\text{Mn}^{4+}$ ), which can have a significant role in

accomplishing the catalytic cycle enhancing the NO oxidation, the nitrate formation, and the  $\text{NH}_3$  activation steps.<sup>11–15</sup> Furthermore, Mn is less toxic than other transition metals like V, Co, and Ni and is highly abundant in soil.

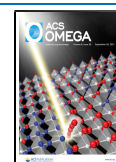
The  $\text{NH}_3$ -SCR cycle typically involves the adsorption and activation of both NO and  $\text{NH}_3$  molecules on the catalyst active sites.<sup>10,16</sup> Optimizing the interaction between the two activated molecules is crucial to avoid undesired parallel reactions, most notably  $\text{NH}_3$  overoxidation and  $\text{N}_2\text{O}$  production.<sup>17,18</sup>

The need of satisfactory catalytic activity can be fulfilled by tailoring the textural features of the support and the redox properties of the active species. The main principle is that the catalyst should be dispersed on a suitable support to obtain stable active species. In addition, it is important that there is adequate metal-support interaction and optimum performance

Received: June 16, 2021

Accepted: August 6, 2021

Published: September 14, 2021



at low metal loading, which consequently reduces the cost of the catalyst. Impregnation and coprecipitation methods are applied to produce a wide range of materials but usually provide a poor control on the formed species and their dispersion and on their interaction with the support. Among the different oxides used as a support for the SCR catalyst,  $\text{TiO}_2$  offers excellent dispersion of the active components, proving to be an ideal candidate support for Mn-based low-temperature SCR catalysts.<sup>15</sup>

Ettireddy et al. explored the effect of Mn loading by wet impregnation of different  $\text{TiO}_2$  phases: anatase was identified as the best support with an optimal Mn content of about 17 wt %, corresponding to monolayer coverage.<sup>19</sup> On the other hand, plentiful papers in the literature report that significant  $\text{NO}_x$  conversion and  $\text{N}_2$  selectivity are obtained by using catalysts having Mn loading larger than 15 wt %.<sup>20,21</sup>

Bimetallic systems are often used to improve the catalytic performance. Putluru et al. prepared a series of Mn/ $\text{TiO}_2$  and Fe-promoted Mn/ $\text{TiO}_2$  catalysts by both precipitation and impregnation methods, and the results were discussed by directly comparing their activity with that of commercial  $\text{V}_2\text{O}_5\text{--WO}_3/\text{TiO}_2$  (3 wt %  $\text{V}_2\text{O}_5$ , 7 wt %  $\text{WO}_3$ ).<sup>22</sup> The catalysts prepared by precipitation exhibited superior low temperature activity with respect to the impregnated ones, reaching 96% NO conversion with an Fe-promoted Mn/ $\text{TiO}_2$  catalyst. Nevertheless, the required total active metal content was 25 wt %, whereas NO conversion values dropped to 65% for a metal content below 10 wt %.

In this scenario, the sol–gel method is an outstanding route providing a potential control of the doping process. Sol–gel is a wet chemical process where a liquid “sol” transforms into a “gel” phase by competition, at the molecular level, between the reactions responsible for the formation and the growth of colloidal particles.

Its versatility and mild conditions allow for tailoring the textural and surface properties through the synthesis parameters, making the sol–gel processing a powerful tool for the synthesis of materials.<sup>23–30</sup>

A superior dispersion with no detectable sintering or formation of  $\text{MnO}_x$  crystalline phases up to a Mn/Ti molar ratio equal to 0.4 was obtained by traditional sol–gel preparation. Nevertheless, the initial expectations of an improved catalytic activity at Mn loading below 20 wt % were not met.<sup>31</sup> The same authors also explored the effect of transition metals in addition to Mn/ $\text{TiO}_2$ -based catalysts for low temperature SCR. Activity was enhanced by adding Fe [ $\text{Fe}(0.1)\text{--Mn}(0.4)/\text{TiO}_2$ ] via the one pot sol–gel procedure, and the NO conversion was more than 90% at about 100 °C.<sup>13</sup>

The work by Kim et al.<sup>32</sup> aimed at investigating the effect of the preparation method on the  $\text{deNO}_x$  activity of the Mn/ $\text{TiO}_2$ -based catalyst. The sol–gel approach allowed for reaching a better  $\text{deNO}_x$  performance as compared to an impregnated Mn/ $\text{TiO}_2$  catalyst in the 150–350 °C temperature range. At 250 °C, 90% NO conversion was achieved with the sol–gel catalyst at the highest Mn content (30 wt %). The observed enhancement of the  $\text{deNO}_x$  activity due to the increase in the Mn content was ascribed to the remarkable dispersion of  $\text{MnO}_2$  on the catalyst surface by the efficient incorporation of Mn into the  $\text{TiO}_2$  matrix during the sol–gel preparation.<sup>32</sup>

Although sol–gel catalysts are more efficient with respect to those obtained by conventional methods (e.g., impregnation), several shortcomings of the reported systems still need to be

addressed, including the narrow temperature range, the substantial Mn content, and to some extent, the low  $\text{N}_2$  selectivity.

Among the different types of chemical processes that may be considered under the heading of “sol–gel”, the reverse micelle approach provides a favorable microenvironment to control the nucleation and growth of nanoparticles (NPs), simultaneously enhancing the metal dispersion. Reverse micelles are nanometric droplets of the aqueous phase stabilized by surfactants in an organic phase, and the rate of hydrolysis and condensation are driven by the frequency of intermicellar exchanges and by the water content in the micelle core, in addition to the structure-directing role of the surfactant. The supramolecular template sol–gel technique overcomes the obstacles encountered in more traditional procedures, where the high hydrolysis rate makes the handling of transition metal alkoxides not straightforward. In addition, transition metals often exhibit several (stable) coordination states, and when coordinatively unsaturated, they are able to expand their coordination sphere by solvation or alkoxy bridging.<sup>33</sup> The vigorous reaction of Ti alkoxides with water leads to (undesired) formation of Ti oxo/hydroxo precipitates. The most common inhibitors are complexing ligands,  $\beta$ -diketones, polyhydroxy acids, or carboxylic acids, which reduce the reactivity of Ti alkoxides by increasing its coordination number and decreasing the number of easily hydrolyzable groups.<sup>33</sup>

In this work, a one-pot reverse micelle strategy has been adopted to prepare  $\text{TiO}_2$ -supported  $\text{MnO}_x$  species at low metal content (namely, 1, 5, and 10 wt % Mn). A thorough physicochemical characterization was carried out by X-ray diffraction (XRD) followed by Rietveld refinement, microRaman spectroscopy,  $\text{N}_2$  isotherm measurement at  $-196$  °C, energy-dispersive X-ray (EDX) analysis, DR (diffuse reflectance) UV–vis spectroscopy, temperature-programmed reduction (TPR) technique, and X-ray photoelectron spectroscopy (XPS) to gain insights into both structural and surface properties of the  $\text{MnO}_x\text{--TiO}_2$  catalysts. The activity in the SCR of  $\text{NO}_x$  with  $\text{NH}_3$  was evaluated by directly comparing the sol–gel  $\text{MnO}_x\text{--TiO}_2$  catalysts with a catalyst prepared by impregnating with the same Mn precursor the (undoped)  $\text{TiO}_2$  prepared by the same reverse micelle sol–gel method. The results were discussed in relation with the structural and surface features, in order to explain the enhanced performance of the sol–gel-derived catalysts, in terms of both low  $T$  activity and low Mn content, obtained during the  $\text{NH}_3$  SCR catalytic tests.

## 2. RESULTS AND DISCUSSION

**2.1. Structural and Textural Properties of the Catalysts.** The diffraction patterns of the various catalysts, displayed in Figure 1, reveal the occurring phases. At a first glance, all the studied samples are multiphase, with anatase (A) as the main phase along with the presence of minor phases, which are labeled B (for brookite), R (for rutile), and P (for pyrolusite, i.e.,  $\beta\text{-MnO}_2$ ); furthermore, the pronounced broadness of the XRD peaks suggests a low degree of crystallinity, that is, a nanometric crystal size of the various phases.

The amount of each phase, the anatase cell parameters, and the crystal size were determined by Rietveld refinement (data shown in Table 1). Due to their low content, for the minor phases, the only refined parameter was their amount, whereas the other parameters were kept constant or equal to anatase,

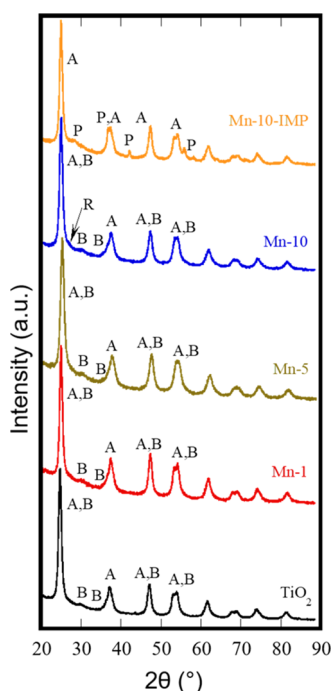


**Figure 1.** XRPD patterns of the prepared samples; the different crystalline phases are labeled as follows: (A) anatase, (B) brookite, (R) rutile, and (P) Pyrolusite.

when possible. The plots of the refinements (data not shown) confirm the very good quality of all the refinements as confirmed by the values of sigma and  $R_{wp}$  (weighted profile R-factor) reported in Table 1.

According to the data given in Table 1, the phase composition of the sol–gel samples is almost the same up to 5 wt % Mn, whereas with the Mn-10 catalyst, the appearance of rutile induces a non-negligible reduction of the anatase content. This finding is not surprising, considering that the Mn dopant addition is reported to promote the anatase to rutile (ATR) phase transformation.<sup>34</sup> With all these catalysts, no trace of Mn-containing crystalline phases was detected. The anatase lattice parameter suggests that at least a certain amount of  $Mn^{4+}$  ions has been dissolved in the anatase matrix by substituting  $Ti^{4+}$  cations. Figure 2 shows that  $TiO_2$  and Mn-1 have a very similar unit cell, in agreement with the low Mn content of the latter sample, and then, a progressive shrinking of the unit cell occurs, perfectly compatible with a partial substitution of  $Ti^{4+}$  ions (octahedral  $Ti^{4+}$  has  $r = 0.605 \text{ \AA}^{35}$ ) by  $Mn^{4+}$  ions (octahedral  $Mn^{4+}$  has  $r = 0.53 \text{ \AA}^{35}$ ). Therefore, by

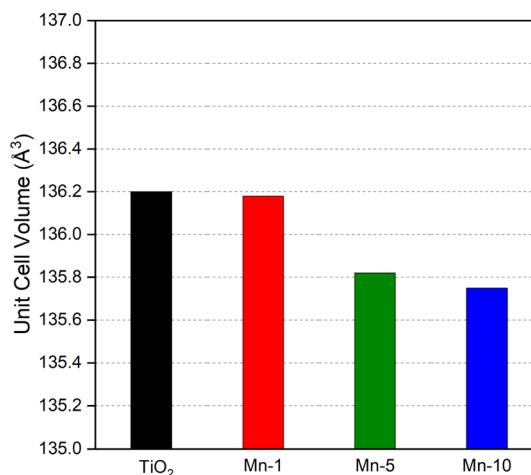


**Figure 2.** Anatase unit cell volume of the sol–gel prepared samples.

increasing the amount of Mn in the sol–gel process, the metal tends to dissolve within the anatase phase. The impregnated sample has a completely different behavior; indeed,  $TiO_2$  is present only as an anatase phase, likely due to the calcination step following the impregnation, whereas Mn occurs in the pyrolusite ( $\beta\text{-MnO}_2$ ) phase. The amount of pyrolusite calculated by Rietveld refinement (almost 9 wt %) is very close to the nominal one (10 wt %), indicating that only a small (if any) fraction of Mn was dissolved in the  $TiO_2$  matrix, in agreement with the adopted (impregnation) procedure.

As a further confirmation, the anatase cell volume of Mn-10-IMP is similar to that of the  $TiO_2$  support, likely indicating that in the impregnated sample, the two oxides crystallized independently and no solid solution of  $MnO_2$  in  $TiO_2$  formed. Therefore, the insertion of Mn inside the anatase lattice is possible only if the system is mixed at an atomic level (here, during the reverse micelle-assisted sol–gel synthesis) and not when mixing occurs at a large scale, as during impregnation.

The reported XRD results strongly evidence the effectiveness of the reverse micelle sol–gel approach where the nanometer-size aqueous systems promote the intimate contact between the precursors. The surfactant, indeed, provides a cage-like environment that favors an excellent control of the final powder stoichiometry with the possibility of obtaining homogeneity and mixing at the atomic scale, ultimately favoring the inclusion of Mn in the studied samples.

The Raman spectra of the prepared catalysts are shown in Figure 3a,b 100–275 and 275–1200  $\text{cm}^{-1}$  range: the typical anatase  $TiO_2$  Raman scattering peaks (black line, Figure 3a,b)

**Table 1.** Determination of Anatase Cell Parameters, Different Phase Contents, and Crystal Size as Obtained by Rietveld Refinement

|   | $TiO_2$ | Mn-1     | Mn-5     | Mn-10    | Mn-10-IMP |
|---|---------|----------|----------|----------|-----------|
| a (Å) anatase                           | 3.78898 | 3.789194 | 3.787906 | 3.78774  | 3.787105  |
| b (Å) anatase                           | 9.48788 | 9.483329 | 9.468461 | 9.463282 | 9.484697  |
| cell volume ( $\text{\AA}^3$ )          | 136.21  | 136.16   | 135.86   | 135.77   | 136.03    |
| anatase (wt %)                          | 91      | 90.49    | 91.23    | 86.19    | 91.42     |
| brookite (wt %)                         | 9       | 9.51     | 8.77     | 10.7     |           |
| rutile (wt %)                           |         |          |          | 3.11     |           |
| pyrolusite (wt %)                       |         |          |          |          | 8.57      |
| crystal size anatase ( $\text{\AA}^3$ ) | 163     | 179      | 153      | 162      | 190       |
| sigma                                   | 1.98    | 1.63     | 1.71     | 1.57     | 1.89      |
| $R_{wp}$                                | 4.27    | 4.34     | 4.23     | 3.65     | 4.17      |



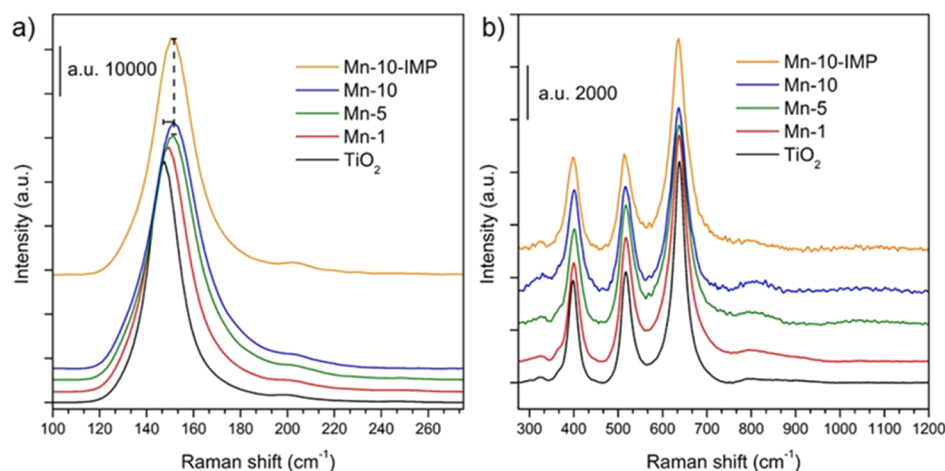


**Figure 3.** Raman spectra of the following samples: TiO<sub>2</sub> (black curve); Mn-1 (red curve), Mn-5 (green curve), Mn-10 (blue curve), and Mn-10-IMP (orange curve). The spectra are reported in two (complementary) sections, (a) (100–275) and (b) (275–1200 cm<sup>−1</sup>) in order to allow the reader to appreciate scattering bands with very different intensities.

are seen at 144 (E<sub>g</sub>), 198 (E<sub>g</sub>), 320 (one of the weak two-phonon bands), 397 (B<sub>1g</sub>), 516 (A<sub>1g</sub> + B<sub>1g</sub>), 639 (E<sub>g</sub>), and 795 (B<sub>1g</sub>) cm<sup>−1</sup>.<sup>36</sup> Some weak signals, due to the low content of brookite TiO<sub>2</sub> and superimposed to the anatase spectrum, are discernible at 247 (A<sub>1g</sub>), 322 (B<sub>1g</sub>), 366 (B<sub>2g</sub>) cm<sup>−1</sup>, as well. In addition, the known<sup>36</sup> strongest modes of brookite at 128 (A<sub>1g</sub>) and 636 (A<sub>1g</sub>) cm<sup>−1</sup> are completely hidden by the nearly coincident modes of anatase.

For all the TiO<sub>2</sub> phases, the modes below 400 cm<sup>−1</sup> are ascribable to O–Ti–O bending vibrations and the ones above 400 cm<sup>−1</sup> are due to Ti–O stretching vibrations. Thus, both types of modes could be affected by the possible incorporation of Mn. In particular, the most sensitive one is the E<sub>g</sub> peak at 144 cm<sup>−1</sup>, as it is much responsive to local oxygen coordination surrounding the metal ion. Actually, as shown in Figure 3a, the blue shift (i.e., toward higher wavenumbers) of the 144 cm<sup>−1</sup> peak, which also becomes asymmetric and larger, increases with the Mn content for the sol–gel catalysts, owing to the disruption of the topological order in the TiO<sub>2</sub> matrix, related to the probable insertion of Mn ions. Moreover, such Mn species could generate point defects in the TiO<sub>2</sub> lattice and its contraction, in agreement with the evolution of such bands.<sup>37</sup> Moreover, by comparing the Mn-10 spectrum (blue line) with Mn-10-IMP (orange line), a shift of the 144 cm<sup>−1</sup> peak occurs (Figure 3a), similar to the one observed for the Mn-5 sample, but the peak does not lose its symmetry. For this reason, the broad anatase peak centered at 198 cm<sup>−1</sup> becomes more intense and, finally, Mn incorporation cannot be inferred by Raman spectroscopy.

Because the modes of the vibrations due to MnO<sub>2</sub> and Mn<sub>2</sub>O<sub>3</sub> species are overlapped to those of TiO<sub>2</sub> in the same spectral region, a subtraction (Figure S1) of the undoped TiO<sub>2</sub> spectrum to each of the Mn-doped TiO<sub>2</sub> spectra has been performed, in order to single out any Mn-related bands. In Figure 3b, the 530 and 651 cm<sup>−1</sup> peaks (related to amorphous MnO<sub>2</sub> and Mn<sub>2</sub>O<sub>3</sub>, respectively) are visible with the Mn-1, Mn-5, and Mn-10 samples.<sup>37</sup> Their intensities increase with the Mn nominal content. With Mn-10, the 318 and 382 cm<sup>−1</sup> modes, assigned to Mn<sub>2</sub>O<sub>3</sub>, are observable,<sup>38</sup> and for Mn-5 and Mn-10, a broad band centered at 1050 cm<sup>−1</sup> related to amorphous MnO<sub>2</sub> appears. The Mn-10-IMP spectrum is quite superimposable to the undoped TiO<sub>2</sub> spectrum (no peak shift

nor width enlargement are observable), and it does not show MnO<sub>x</sub>-related modes, except for the very broad signal at 1050 cm<sup>−1</sup>. Moreover, no trace of pyrolusite, instead detected by XRD, could be singled out (the reference RRUFF Project Raman pyrolusite spectrum being not reported), thus suggesting that the formed Mn oxides (detected by both XRD and DR-UV–vis spectroscopy, *vide infra*) are not homogeneously dispersed on the surface of TiO<sub>2</sub> and/or that their amount is below the sensitivity of the Raman technique in the examined spots. This result confirms that impregnation does not allow a fine dispersion of Mn on the sample, whereas the sol–gel method does. Indeed, the EDX analysis (Table 2)

**Table 2.** Textural Properties of the Studied Samples as Determined by N<sub>2</sub> Isotherms at −196 °C, FESEM and EDX Analyses

| sample           | BET SSA (m <sup>2</sup> g <sup>−1</sup> ) | total pore volume (cm <sup>3</sup> g <sup>−1</sup> ) | micropore volume <sup>a</sup> (cm <sup>3</sup> g <sup>−1</sup> ) | EDX (nominal) Mn/Ti atomic ratio |
|------------------|---|--|--|----------------------------------|
| TiO <sub>2</sub> | 70  | 0.090  | 0.0002   |                                  |
| Mn-1             | 57  | 0.096  | 0.0017   | 0.0164(0.0147)                   |
| Mn-5             | 76  | 0.109  | 0.0017   | 0.0656(0.0765)                   |
| Mn-10            | 68  | 0.102  | 0.0004   | 0.106(0.161)                     |
| Mn-10-IMP        | 40  | 0.070  |  | 0.604 (0.161)                    |

<sup>a</sup>As obtained according to the *t*-plot method.

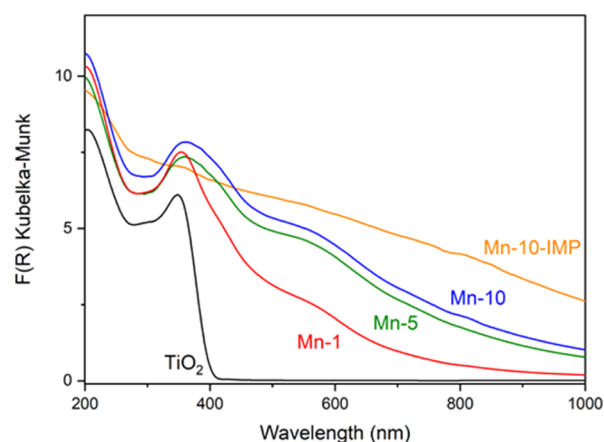
shows Mn/Ti atomic ratios close to nominal values for the sol–gel catalysts, whereas the value determined with the impregnated sample is very high, likely due to the aforementioned heterogeneity induced by the impregnation technique.

Table 2 also reports the textural properties of the catalysts as obtained by N<sub>2</sub> physisorption at −196 °C. The samples showed type IV isotherms (Figure S2) with a H2 hysteresis loop, characteristic of mesoporous solids with interparticle porosity. As expected, the impregnated sample shows a drop in both the surface area and pore volume, whereas the other samples show Brunauer–Emmett–Teller (BET) specific surface area (SSA) values in the 57–76 m<sup>2</sup> g<sup>−1</sup> range and total pore volume values in the 0.09–0.102 cm<sup>3</sup> g<sup>−1</sup> range, indicating a limited effect of Mn doping on the sample porosity.

The field-emission scanning electron microscopy (FESEM) analysis (Figure S3) showed the occurrence of spherical NPs with uniform shape and size, forming large agglomerates/aggregates, likely due to NP coalescence after calcination. The Mn-10-IMP sample showed instead larger NPs but still with a quasispherical shape and forming large agglomerates/aggregates.

## 2.2. Characterization of Bulk and Surface Mn Species.

The DR UV–vis spectra of the studied catalysts are reported in Figure 4. As expected, TiO<sub>2</sub> shows a typical UV–vis spectrum



**Figure 4.** DR UV–vis spectra of the following samples: TiO<sub>2</sub> (black curve); Mn-1 (red curve), Mn-5 (green curve), Mn-10 (blue curve), and Mn-10-IMP (orange curve).

due to the CT (charge-transfer) transitions from O<sup>2−</sup> to Ti<sup>4+</sup>: a band gap ( $E_g$ ) of 3.01 eV has been calculated by applying the Tauc's plot method and assuming an indirect semiconductor behavior  $(F(R)(h\nu))^{1/2}$  in agreement with the fact that it mainly contains anatase (indirect semiconductor), with a minor amount of brookite (direct semiconductor). The DR UV–vis spectrum of Mn-10-IMP, instead, shows a broad absorption in the whole investigated range and resembles the literature spectra usually reported for MnO<sub>2</sub>.<sup>39</sup> This result is in agreement with XRD patterns (*vide supra*), showing the occurrence of pyrolusite in the sample.

Considering the Mn-doped catalysts obtained by sol–gel, the Mn-1 spectrum shows two broad and intense absorptions at about 420 and 560 nm, that is, in the region of Mn ion d–d transitions (360–800 nm). At higher Mn contents (i.e., Mn-5 and Mn-10 spectra), the two bands become more intense, another component is observed at ca. 390 nm, and simultaneously, the O<sup>2−</sup> to Ti<sup>4+</sup> CT band (at 350 nm in TiO<sub>2</sub>) suffers a slight red shift (i.e., toward longer wavelength), likely due to Mn doping by inclusion in the TiO<sub>2</sub> lattice, as shown by XRD. The component at 390 nm is assigned in the literature to d–d transitions of octahedral Mn<sup>4+</sup> ions,<sup>40</sup>

whereas the other two bands are ascribed to different MnO<sub>x</sub> species, likely amorphous (as confirmed by both XRD and Raman techniques) and located at the NP surface, in agreement with XPS results (*vide infra*).<sup>41</sup>

The catalysts prepared by sol–gel synthesis show a progressive decrease of the  $E_g$  value to 2.06 (Mn-1), 1.64 (Mn-5), and 2.00 eV, (Mn-10) confirming that, along with the formation of surface MnO<sub>x</sub> species, bulk Mn doping occurs by using the adopted synthesis technique, in agreement with XRD results (*vide supra*). Moreover, this result is in agreement with both experimental<sup>42</sup> and theoretical studies,<sup>43</sup> the latter showing that substitution of Ti<sup>4+</sup> ions by Mn ions leads to a remarkable red shift of the optical absorption edge both by overall reduction of the band gap and introduction of curvy intermediate bands into the forbidden gap. The (unexpected) increase of the band gap energy with the Mn-10 sample may be due to an extensive doping, which can lead to the well-known Moss-Burnstein effect occurring at a high dopant content. Indeed, with Mo-doped TiO<sub>2</sub> samples with the similar metal content obtained by the same synthesis procedure,<sup>44</sup> the same effect was observed; this result is another proof of the effectiveness of the sol–gel synthesis in the doping of TiO<sub>2</sub> by heteroatom ions (here, Mn).

The surface chemical composition of the Mn-doped TiO<sub>2</sub> catalysts has been investigated by means of XPS, allowing for both a qualitative and quantitative analysis of the surface chemical composition. Table 3 reports the surface elemental composition (at. %) along with the Mn/Ti atomic ratios, as derived by the quantification of the O 1s, Mn 2p, and Ti 2p spectral regions.

The surface amount of Mn was found to increase with the nominal Mn content, as shown by both the absolute Mn at. % and the Mn/Ti atomic ratio values reported in Table 3, in agreement with a previous work concerning Mo-doped TiO<sub>2</sub> samples obtained by means of the same synthetic procedure.<sup>44,45</sup> Also, the impregnation procedure resulted in a higher surface Mn availability, as compared to the sol–gel process, as seen by comparing the Mn/Ti ratio of the Mn-10-IMP and the Mn-10 samples.

In order to gather information on the surface chemical speciation and Mn oxidation states, a curve-fitting procedure was applied to the Ti 2p, Mn 2p, and O 1s high-resolution XP spectra. The Ti 2p spectral region showed the typical spin–orbit splitting doublet of Ti 2p<sub>3/2</sub> and Ti 2p<sub>1/2</sub> species with binding energy (BE) and separation values consistent with Ti<sup>4+</sup> in the TiO<sub>2</sub> lattice (Figure S4). The Mn 2p and O 1s XP regions (Figures 5 and 6, respectively) provided interesting results on the possible oxidation states of Mn and oxygen surface vacancies.

Mn 2p XP spectra can be very complex due to the coupling of angular momenta associated with partially filled core and valence shells containing unpaired electrons. This can create a

**Table 3.** XPS Surface Elemental Composition of Mn-Doped TiO<sub>2</sub> Catalysts. The Values are Averaged out of at Least Three Replicates and are Reported as Mean Value  $\pm$  1S

| Sample    | XPS surface elemental composition (at. %) |                |                |                    |
|-----------|---|----------------|----------------|--------------------|
|           | Mn  | Ti             | O              | Mn/Ti atomic ratio |
| Mn-1      | 1.1 $\pm$ 0.2                             | 26.5 $\pm$ 1.6 | 72.4 $\pm$ 1.6 | 0.042 $\pm$ 0.004  |
| Mn-5      | 2.6 $\pm$ 0.3                             | 26.3 $\pm$ 1.1 | 71.1 $\pm$ 1.4 | 0.10 $\pm$ 0.01    |
| Mn-10     | 3.5 $\pm$ 0.5                             | 24 $\pm$ 2     | 73 $\pm$ 2     | 0.15 $\pm$ 0.02    |
| Mn-10-IMP | 10.5 $\pm$ 0.5                            | 17.5 $\pm$ 1.0 | 72.3 $\pm$ 1.3 | 0.58 $\pm$ 0.04    |

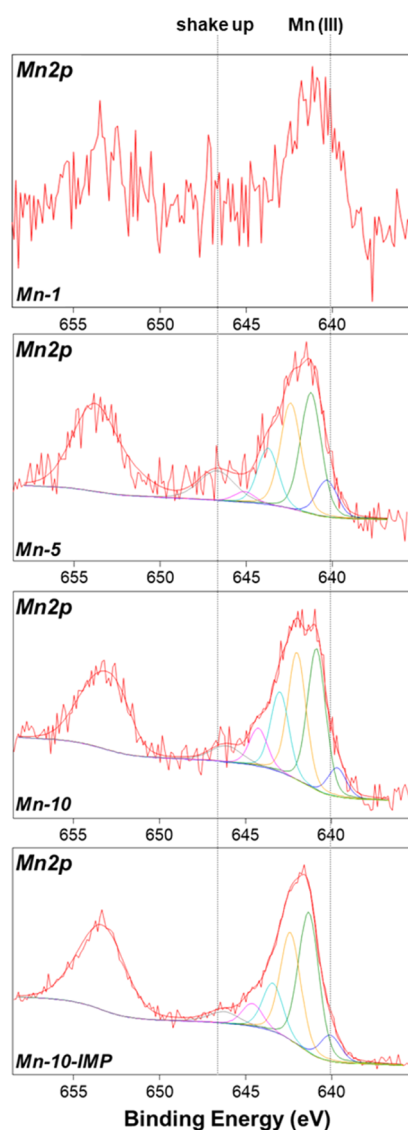


**Figure 5.** Mn 2p XP spectra for all Mn-doped catalysts. Curve fitting has been applied only to the  $2p_{3/2}$  peak component.

number of final states, which will manifest in the XP spectrum in the form of multiplet splitting. In particular, out of the six stable manganese oxidation states (0, +2, +3, +4, +5, and +7), three have significant multiplet splitting ( $\text{Mn}^{2+}$ ,  $\text{Mn}^{3+}$ , and  $\text{Mn}^{4+}$ ), and thus, the qualitative and quantitative XPS investigation of Mn-containing samples is particularly challenging.<sup>11,46–49</sup> The separation of the  $2p_{3/2}$  and  $2p_{1/2}$  spin–orbit splitting components of Mn is large enough to consider only the (more intense)  $2p_{3/2}$  signal and its associated structure.

The curve fitting procedure applied to the Mn  $2p_{3/2}$  XP spectra of Mn-1 to Mn-10-IMP samples is reported in Figure 5. Due to the complexity of this signal, a first parameter to focus on could be the main peak shape because it presents some detailed features depending on the presence/prevalence of the specific oxidation state, as described by Biesinger et al. who reported Mn 2p spectra for various standard samples and discussed in detail the corresponding fitting parameters.<sup>46</sup> Comparing the Mn 2p spectra of the present work with those by Biesinger et al., it is possible to observe the occurrence of a shake-up satellite around  $646.0 \pm 0.2$  eV, suggestive of surface Mn(II) species, whose relative abundance decreases as the

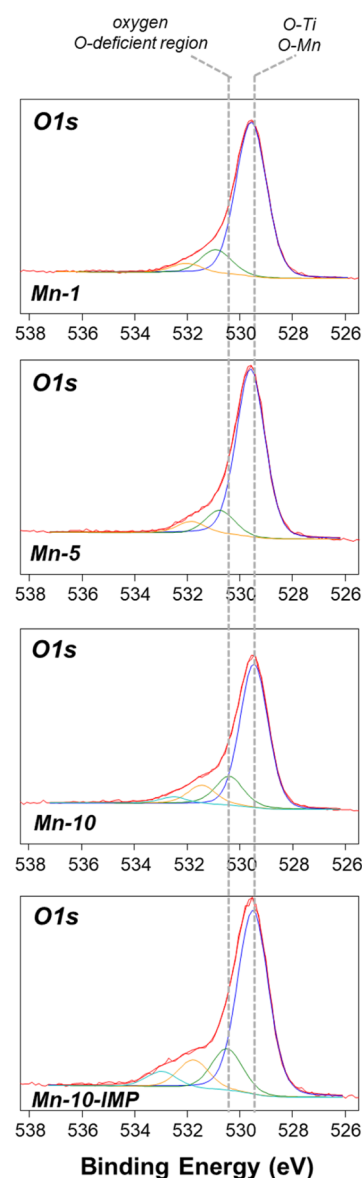


**Figure 6.** O 1s XP spectra and corresponding curve fittings as obtained with the samples (from top to bottom): Mn-1, Mn-5, Mn-10, and Mn-10-IMP.

total Mn % increases (see Table S1 in the Supporting Information file). It is close to 9% in the Mn-5 sample and goes down to 3% in the Mn-10-IMP sample. Also, a prominent shoulder at lower BE values ( $640.0 \pm 0.2$  eV), typical of Mn(III), could be identified in all the samples with a comparable relative abundance. With the Mn-10-IMP sample, it is also possible to identify a peak shape and a multiplet splitting strongly resembling those of Mn(III) species. The Mn  $2p_{3/2}$  XP spectrum of Mn-1 was not curve fitted, due to the very low signal-to-noise ratio, but the general peak shape is close to those of both Mn-5 and Mn-10. A further spectral feature is the 2p spin–orbit splitting value; it is shown to increase as the Mn oxidation state increases.<sup>17</sup> The value for all our catalysts is always  $11.6 \pm 0.1$  eV, compatible with the presence of both Mn(II) and Mn(III). All those findings indicated that a mix of Mn(II) and Mn(III) is generally distinguishable at the surface of the Mn-doped catalysts: Mn(II) species could be hypothesized to be more abundant in the case of the sol–gel samples and their relative amount



decreasing at a higher Mn content; conversely, Mn(III) species are predominant at the surface of the impregnated catalyst. Moreover, due to complexity of Mn 2p multiplet splitting, the occurrence of small amounts of Mn(IV) species could not be excluded, especially in the Mn-10-IMP sample on the base of the main peak shape. All these experimental evidences are confirmed by TPR analysis (*vide infra*).

The curve-fitted O 1s XP spectra are reported in Figure 6; the curve fittings shown from three (with the Mn-1 and Mn-5 samples) to four peak components (with the Mn-10 and Mn-10-IMP samples). The lowest BE peak is due to lattice oxygen species bonded to Ti and/or Mn ( $529.7 \pm 0.2$  eV), whereas the BE peak at around  $531.4 \pm 0.3$  eV is attributed to nonlattice oxygen/OH species. Finally, the component at  $530.5 \pm 0.1$  eV is due to oxygen in oxygen-deficient regions, whereas the highest BE peak (at  $533.2 \pm 0.2$  eV) is ascribed to adsorbed/structural water.<sup>50,51</sup> It is important to notice how the amount of oxygen vacancies increases with the dopant concentration, as can be derived by the relative abundance of the peak component at  $530.5 \pm 0.1$  eV, which is around 10–11% in Mn-5 and increases up to 16% in Mn-10 and Mn-10-IMP. As a whole, XPS analysis showed the occurrence of surface Mn species at the variable oxidation state [Mn(II) species being mainly found on the samples prepared by sol-gel]. Correspondingly, oxygen vacancies are observed due to the charge balance. Their occurrence in the Mn-10-IMP sample shows that the surface composition of pyrolusite differs from that of its bulk because only Mn<sup>2+</sup> and Mn<sup>3+</sup> species are observed by XPS.

Moreover, comparison of the Mn/Ti atomic ratio at the surface (XPS) and in the bulk (EDX) shows the occurrence of a surface enrichment in Mn, as previously observed with another set of Mo-doped TiO<sub>2</sub> samples with the similar heteroatom content that were obtained by the same synthesis procedure.<sup>44</sup>

The occurrence of different redox species and their dispersion at the catalyst surface is notoriously one of the main factors controlling the catalytic activity in the studied reaction. The redox ability of the catalysts was investigated by H<sub>2</sub>-TPR, and the corresponding results are shown in Figure 7. The amount of H<sub>2</sub> consumption, reported in the following paragraphs, has been calculated in the range between room temperature and 500 °C.

According to the literature, the reduction process of manganese oxides covers a broad temperature range where (bulk) MnO<sub>2</sub> is successively reduced to lower oxidation states in the order MnO<sub>2</sub> → Mn<sub>2</sub>O<sub>3</sub> → Mn<sub>3</sub>O<sub>4</sub> → MnO. The following *T* ranges are usually reported for the reduction of manganese oxides: 290–350 °C for MnO<sub>2</sub> reduction (but for pyrolusite, β-MnO<sub>2</sub>, the *T* range increases up to 430 °C), 350–420 °C for Mn<sub>2</sub>O<sub>3</sub> reduction to Mn<sub>3</sub>O<sub>4</sub>, and 450–500 °C for Mn<sub>3</sub>O<sub>4</sub> reduction to MnO, which is not further reducible at the partial pressure of H<sub>2</sub> adopted during TPR analysis.<sup>19,22,52,53</sup> Reducibility is significantly affected by several other variables, like oxide dispersion and crystallite size, interaction with the support, synthesis method, and so forth.<sup>19</sup>

The undoped TiO<sub>2</sub> (not reported) showed some H<sub>2</sub> consumption, in agreement with the literature reporting that the support is not inert toward reduction.<sup>54,55</sup> In the TPR profile of the Mn-10-IMP catalyst (Figure 7), two sharp and well-defined reduction peaks were observed at ca. 325 and 435 °C, respectively. At higher *T*, no further peaks, ascribable to TiO<sub>2</sub> reduction, were identified. The TPR spectrum of Mn-10-

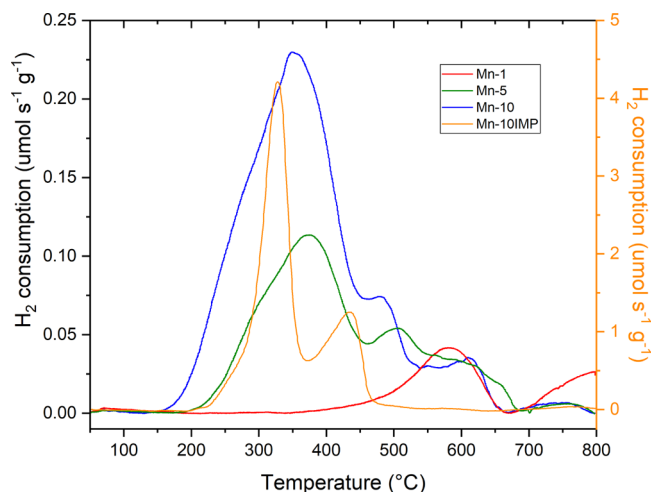


**Figure 7.** H<sub>2</sub>-TPR profiles reported for the following samples: Mn-1 (red curve), Mn-5 (green curve), Mn-10 (blue curve), and Mn-10-IMP (orange curve). The left Y axis refers to the Mn-1, Mn-5, and Mn-10 samples; and the right Y axis refers to the Mn-10-IMP sample.

IMP likely corresponds to the reduction of MnO<sub>2</sub> to MnO, suggesting the following two-step reduction process: MnO<sub>2</sub> → Mn<sub>2</sub>O<sub>3</sub>/Mn<sub>3</sub>O<sub>4</sub> and Mn<sub>2</sub>O<sub>3</sub>/Mn<sub>3</sub>O<sub>4</sub> → MnO.<sup>56</sup> The related H<sub>2</sub> consumption was 91.8 μmol g<sup>-1</sup>, which corresponded to a Mn average oxidation state of 3.9, in good agreement with XRD results, where crystalline β-MnO<sub>2</sub> was detected. The Mn-10 sample also showed two reduction peaks in the 250–550 °C range, indicating a two-step reduction process; however, the peaks were shifted to higher *T* as compared to the Mn-10-IMP sample, indicating an overall lower average Mn oxidation state.<sup>57</sup> This hypothesis is confirmed by the H<sub>2</sub> consumption that for the Mn-10 sample dropped to 16.3 μmol g<sup>-1</sup>, from which an average Mn oxidation state of 2.5 was calculated. Moreover, the shape of the overall TPR profile is very broad and structured as compared to the Mn-10-IMP sample, indicating the likely occurrence of several nonstoichiometric MnO<sub>x</sub> species, in agreement with Raman spectroscopy.<sup>57</sup>

Concerning the H<sub>2</sub> consumption above 500 °C, the peak at ca. 600 °C is due to the formation of Ti<sup>3+</sup> species, forming oxygen deficient TiO<sub>x</sub> species, whereas the minor H<sub>2</sub> consumption at c.a. 750 °C could be assigned to the reduction of the brookite phase, although in the same *T* range, other authors pointed out the occurrence of the ATR transition, which hampers a straightforward assignment in this case.<sup>58–60</sup>

The Mn-5 sample showed a H<sub>2</sub> consumption of 9.5 μmol g<sup>-1</sup> corresponding to a calculated Mn average oxidation state of 2.3. The two reduction peaks observed for Mn-5 are even more shifted to higher *T* compared to Mn-10, in agreement with a slightly lower average oxidation state.

The TPR spectrum of the Mn-1 sample showed very low intensity and the amount of consumed H<sub>2</sub> was 1.8 μmol g<sup>-1</sup>, which corresponded to a Mn average oxidation state of 2.3.

As expected, the introduction of Mn by sol-gel synthesis induced a remarkable change in the TPR curve shape and in the H<sub>2</sub> consumption, with respect to the impregnation procedure, being responsible for the formation of a mixture of oxidation states.

The different reducibility of the MnO<sub>x</sub> species, driven also by the strength of the interaction with the support, is responsible of the observed broadened TPR profile. However, the sol-gel method favors a strong Mn–TiO<sub>2</sub> interaction,



likely enhancing the reduction of the  $\text{MnO}_x$  species with respect to unsupported  $\text{Mn}_2\text{O}_3$  and  $\text{Mn}_3\text{O}_4$  with a consequent shift of the reduction onset to lower  $T$  values.<sup>10,27,61</sup> This modulation of Mn reducibility could (positively) affect the  $\text{NO}_x$  catalytic conversion, thus impacting the SCR activity of the Mn-doped  $\text{TiO}_2$  samples.

Another physico-chemical property, which may affect the  $\text{NH}_3$ -SCR catalytic activity, is surface acidity; Figure 8 shows

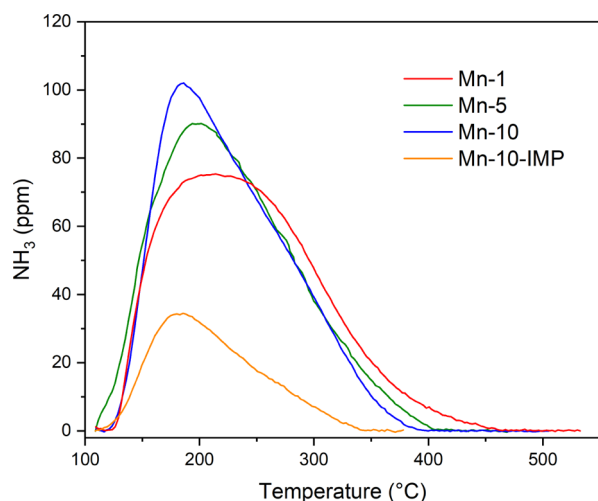


**Figure 8.**  $\text{NH}_3$ -TPD curves of Mn-1 (red curve), Mn-5 (green curve), Mn-10 (blue curve), and Mn-10-IMP (orange curve) as measured in the 100–550  $^{\circ}\text{C}$  range.

the sample  $\text{NH}_3$ -TPD profiles in the 100–550  $^{\circ}\text{C}$  range. With respect to the samples prepared by the reverse micelles sol–gel method, the Mn-10-IMP sample showed a smaller amount of desorbed  $\text{NH}_3$  ( $d_{\text{NH}_3}$ ) per g of the catalyst (i.e., 75  $\mu\text{mol g}^{-1}$ ), in agreement with its smaller SSA value, and a sharper TPD curve in the 125–350  $^{\circ}\text{C}$  range, indicating the occurrence of fewer and weaker acidic sites. The Mn-1 sample ( $d_{\text{NH}_3} = 242 \mu\text{mol g}^{-1}$ ) showed a different shape in a broader  $T$  range (125–450  $^{\circ}\text{C}$ ), indicating the presence of abundant and heterogeneous acidic sites.<sup>20</sup> The Mn-5 ( $d_{\text{NH}_3} = 244 \mu\text{mol g}^{-1}$ ) and Mn-10 ( $d_{\text{NH}_3} = 244 \mu\text{mol g}^{-1}$ ) samples showed very similar features not only in terms of the amount of acidic sites, but also in terms of the broad TPD curve profile extending in a wide  $T$  range, although Mn-5 showed an onset at slightly lower  $T$ . As a whole, the Mn-1, Mn-5, and Mn-10 TPD profiles indicated the occurrence of different types of  $\text{NH}_3$  adsorbed species with different thermal stabilities at the catalyst surface.<sup>62</sup> Concerning the nature of those acidic sites, that is, Brønsted or Lewis sites,  $\text{NH}_4^+$  ions decompose at a lower  $T$  with respect to  $\text{NH}_3$ -Lewis acid site adducts; in agreement with the literature, the desorption at low  $T$  (below 200  $^{\circ}\text{C}$ ) may be assigned to  $\text{NH}_3$  molecules obtained by the decomposition of  $\text{NH}_4^+$  ions bound to Brønsted acid sites and the desorption at high  $T$  is associated with  $\text{NH}_3$  molecules coordinated to Lewis acid sites. The strength of such Lewis acid sites is weak to medium by considering the desorption  $T$  range.<sup>63</sup> Brønsted acid sites are also important for the SCR catalytic activity, and they seem to be more abundant with the Mn-5 sample, showing a desorption onset at a slightly lower  $T$  and a component at ca. 170  $^{\circ}\text{C}$ .

**2.3. Catalytic Activity— $\text{NH}_3$ -SCR.** The results of the catalytic activity, in terms of  $\text{NO}_x$  conversion and  $\text{N}_2$  selectivity, of all the studied catalysts operating under identical experimental conditions are illustrated in Figure 9a,b. All the

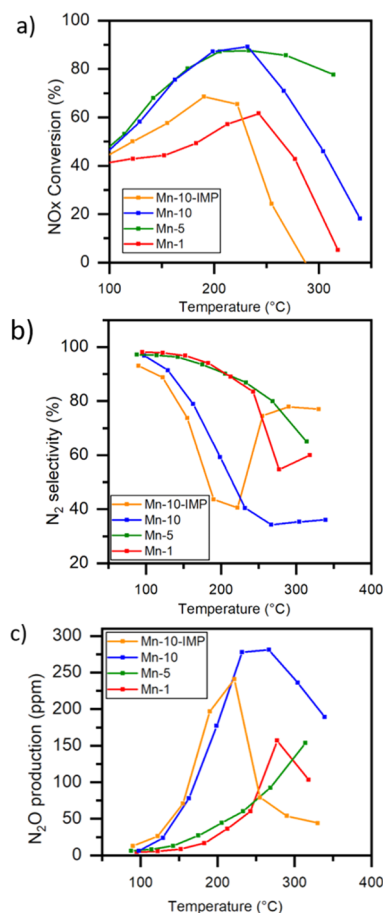
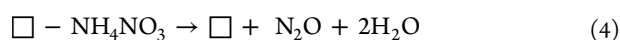
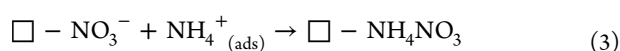
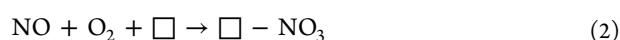
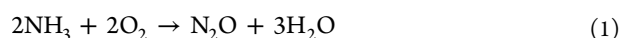


**Figure 9.**  $\text{NO}_x$  conversion (a),  $\text{N}_2$  selectivity (b), and  $\text{N}_2\text{O}$  production (c) over the sol gel synthesized and impregnated samples.

conversion curves presented a similar trend as a function of  $T$ , with a maximum of conversion followed by a more or less pronounced decline, depicting a “bell” or Gaussian shape rather than a sigmoidal one. This behavior is clearly attributed to the competition of the standard SCR reaction with at least two side reactions, namely, the catalytic oxidation of  $\text{NH}_3$  to give either  $\text{N}_2$  or  $\text{N}_2\text{O}$ .<sup>64</sup> In fact, beyond the maximum  $T$ , the  $\text{NH}_3$  oxidation becomes kinetically prevalent, so that the reacting  $\text{NH}_3$  is consumed in side reactions, with a consequent decrease in  $\text{NO}_x$  conversion.

The Mn-5 catalyst showed the best SCR activity, exhibiting both the highest  $\text{NO}_x$  conversion and the lowest amount of  $\text{N}_2\text{O}$  produced in the 200–250  $^{\circ}\text{C}$  range; the conversion was almost 90%; and the  $\text{N}_2\text{O}$  concentration was ca. 50 ppm. The Mn-10 sample had the same  $\text{NO}_x$  conversion as Mn-5; however, the selectivity was much lower (more than five times with respect to the Mn-5 catalyst at the maximum conversion) and high  $\text{N}_2\text{O}$  production was observed, while a lower Mn loading (Mn-1) resulted in lower conversion. With the Mn-10 sample, a rapid increase in the  $\text{N}_2\text{O}$  produced was observed suggesting the prominence of the (parasitic) oxidation of  $\text{NH}_3$  that, being oxidized, did not participate in the SCR reaction and this is likely promoted by the high content of the reducible

Mn species present in the Mn-10 catalyst, meaning an increased oxidative behavior. It has been widely demonstrated that the high activity of the Mn-based SCR catalysts is the result of the high NO oxidation and its subsequent adsorption in the form of  $\text{NO}_{2(\text{ads})}$  over the manganese active sites. Activated ammonia also adsorbs on the same acid sites, and it recombines with nitrites consequently decomposing into  $\text{N}_2$  and  $\text{H}_2\text{O}$ .<sup>65</sup> However, the rate of formation of such intermediates ( $\text{NH}_4\text{NO}_2$  or  $\text{NH}_2\text{NO}$ ) depends on the  $\text{NH}_3$ -SCR reaction rate, that is, favored at low temperatures, in comparison with the nonselective  $\text{NH}_3$  oxidation rate, which prevails at high temperatures.  $\text{N}_2\text{O}$  is produced by either overoxidation of  $\text{NH}_3$  [reaction 1] at higher  $T$  ( $>250$  °C) or formation and decomposition of ammonium nitrate and/or nitrite intermediates at low  $T$  [reactions 2 and 3],<sup>17,18,52,66</sup> as shown in the following set of reactions



where eq 1 represents the ammonia oxidation, eq 2 represents the nitrate formation, eq 3 represents the ammonium nitrate formation, eq 4 represents the ammonium nitrate decomposition, and  $\square$  depicts an active site.

The  $\text{N}_2$  selectivity and  $\text{N}_2\text{O}$  production (Figure 9b,c) was highly dependent on the synthesis method and the Mn loading likely due to the competition between the abovementioned reactions and the SCR reaction. One of the widely accepted theories for the  $\text{TiO}_2$ -based SCR reactions is a bifunctional mechanism whereby  $\text{NH}_3$  is activated over the acid sites predominantly located on the  $\text{TiO}_2$  support with participation of the  $-\text{OH}$  terminations of the metal sites and the subsequent reaction with the nitrates.<sup>65,67</sup> An increase of the metal loading shifts the  $\text{NH}_3$ - $\text{NO}_x$  activation predominantly over Mn, and above a certain amount, the mechanism changes and the ammonium nitrate formation and decomposition [reactions 3 and 4] become the primary SCR pathway, favoring the  $\text{N}_2\text{O}$  production. This hypothesis can explain the drastic change in the  $\text{N}_2$  selectivity for the sol-gel catalysts with 5 and 10 wt % Mn loading (Mn-5 and Mn-10, respectively), which still showed similar overall  $\text{NO}_x$  conversion. In fact, the similar amount and nature of the acid sites, as demonstrated by  $\text{NH}_3$ -TPD reported in Figure 8, justified the very close behavior concerning  $\text{NO}_x$  conversion, correlated to  $\text{NH}_3$  adsorption, while the lower amount and better dispersion of manganese in the Mn-5 catalyst hindered the mechanism of  $\text{N}_2\text{O}$  production previously described and improved the  $\text{N}_2$  selectivity. Finally, above 250 °C, the  $\text{N}_2\text{O}$  production and  $\text{N}_2$  selectivity decreased because the  $\text{NH}_3$  overoxidation produced NO instead of  $\text{N}_2\text{O}$ .

The impregnated sample had much lower  $\text{NO}_x$  conversion and selectivity (i.e., high  $\text{N}_2\text{O}$  produced per NO converted) that could be attributed to the surface occlusion of the  $\text{TiO}_2$  acid sites that typically adsorbs  $\text{NH}_3$  and activates it for the further SCR reaction, in agreement with the overall  $\text{NH}_3$  desorbed amount determined as by  $\text{NH}_3$ -TPD (*vide supra*). As evidenced in the previous sections, the contact and interaction between Mn and Ti superficial active sites were highly improved due to the one-pot synthesis and the resulting high

dispersion of Mn that was not possible to achieve by conventional impregnation. Indeed, the XRD analysis (Figure 1), the Raman spectroscopy (Figure 3) and the DR UV-vis spectroscopy (Figure 4) demonstrated the high Mn dispersion and that after calcination, the  $\text{MnO}_2$  and  $\text{Mn}_2\text{O}_3$  phases remained amorphous in the sol-gel samples with respect to the impregnated sample, where crystalline pyrolusite was detected. The remarkable low-temperature  $\text{NO}_x$  SCR activity can be likely attributed to such increased dispersion and to the enhanced contact between the multiple  $\text{TiO}_2$  and  $\text{MnO}_x$  active sites, where NO and  $\text{NH}_3$  adsorption occurs, therefore interaction and rearrangement toward  $\text{NH}_4\text{NO}_2$  and  $\text{NH}_2\text{NO}$  intermediates can take place more easily, mainly on the amorphous phases, improving the  $\text{NO}_x$  conversion at low temperatures.<sup>68–70</sup>

### 3. CONCLUSIONS

The physico-chemical characterization results showed that the adopted reverse micelle sol-gel synthesis has an impact on the Mn surface and bulk dispersion and on the strength of Mn/ $\text{TiO}_2$  interaction. Specifically, with respect to the traditional impregnation method, the reverse micelle method allowed for a fair dispersion of 1, 5, and 10 wt % Mn both in the bulk and at the surface of  $\text{TiO}_2$  NPs, with surface  $\text{MnO}_x$  species resulting mainly amorphous and characterized by a different redox behavior as compared to those obtained by impregnation (i.e., crystalline pyrolusite).

As compared to the literature, the  $\text{NH}_3$ -SCR catalytic tests showed that the studied catalysts have enhanced  $\text{deNO}_x$  activity in  $\text{NH}_3$ -SCR, notwithstanding the low Mn content; both 5 and 10 wt % Mn catalysts were active at low  $T$ , the best catalytic activity being obtained at 5 wt % nominal Mn content.

The ensemble of the characterization techniques and the catalytic tests allowed for figuring out in the set of studied catalysts and “optimal” Mn content (i.e., nominal 5 wt %), corresponding to a material characterized by abundant and probably weaker (Brønsted) acidic sites and well-dispersed Mn-species. The same surface species were stabilized as the strong interaction with the support, as obtained by the reverse micelle sol-gel synthesis, which also favored the formation of lower oxidation states of Mn, that is, Mn(II) and Mn(III), in the surface amorphous  $\text{MnO}_x$  phases.

As a whole, the reported synthesis procedure could be utilized for those types of application (her,  $\text{NH}_3$ -SCR), requiring the fair dispersion of metal species and their stabilization by the support.

### 4. EXPERIMENTAL SECTION

**4.1. Synthesis Method.** All the chemicals were provided by Sigma-Aldrich (Italy).

Mn-doped and undoped  $\text{TiO}_2$  NPs were prepared by the reverse micelle microemulsion sol-gel method<sup>71</sup> using polyoxyethylene (20) oleyl ether (Brij O20) as a surfactant and cyclohexane as an oil phase, and titanium(IV)butoxide 97% ( $\text{Ti}(\text{BuO})_4$ ) and manganese(II) nitrate tetrahydrate [ $\text{Mn}(\text{NO}_3)_2 \cdot 4\text{H}_2\text{O}$ , *purum* p.a.  $\geq 97\%$ ] as precursors.

In a typical synthesis, a proper amount of Brij-O20 is dispersed in cyclohexane by stirring at 50 °C. Meanwhile,  $\text{Mn}(\text{NO}_3)_2 \cdot 4\text{H}_2\text{O}$  is dissolved in distilled water and the aqueous solution is added to the oil/surfactant solution and stirred for 45 min, with the formation of a water in-oil (w/o)

microemulsion of surfactant nanoreactors. Afterward,  $\text{Ti}(\text{BuO})_4$  is dropwise added to the emulsion.

The mixture is stirred for 2 h at the constant temperature of 50 °C, and finally, the emulsion is broken by the addition of 2-propanol, followed by sonication. The solid phase is then collected by centrifugation and dried at 100 °C for 24 h, followed by calcination in air at 500 °C for 2 h with a temperature ramp of 2.5 °C min<sup>-1</sup>. Proper precursor amounts were used in order to obtain Mn wt % nominal contents of 0 wt % ( $\text{TiO}_2$ ), 1 wt % (Mn-1), 5 wt % (Mn-5), and 10 wt % (Mn-10). Undoped titania was prepared by the same procedure.

For comparison, a sample with a 10 wt % nominal Mn content (Mn-10-IMP) was prepared by the incipient wetness impregnation method by using the same Mn precursor; the support (i.e., the  $\text{TiO}_2$  sample prepared by the reverse micelle sol–gel method) was impregnated with few drops of the Mn precursor aqueous solution under stirring at 80 °C. The resulting powder was then calcined by following the same procedure adopted for the other sol–gel prepared samples.

**4.2. Methods.** X-ray powder diffraction (XRPD) patterns were obtained on an X'Pert Phillips diffractometer operating with Cu  $K\alpha$  radiation (1.541874 Å) and equipped with a PIXcel 1D detector (step: 0.026°2 $\theta$ ; time per step: 2 s). Lattice parameters, crystallite size, and quantitative phase analysis were determined by Rietveld analysis, as implemented in MAUD software.<sup>72</sup> The instrumental broadening was characterized by means of the standard NIST 660a ( $\text{LaB}_6$ ).

Raman spectra were collected by means of a Renishaw InVia Reflex microRaman spectrometer (Renishaw plc, Wotton-under-Edge, UK) equipped with a cooled charge-coupled device camera. The Raman source was a diode-pumped solid-state laser ( $\lambda_{\text{ex}}$  = 514.5 nm), and the sample inspection was performed through a microscope objective (10 $\times$ ) in back-scattering light collection mode. 5 mW laser power, 5 s of exposure time, and four accumulations were employed to collect each spectrum of the pelletized (to facilitate the surface focusing) powders. 0.1 mW laser power was selected for the pelletized (undoped)  $\text{TiO}_2$  powder only to prevent the scattering signal saturation of the detector. For each sample, five spectra have been recorded on different regions of the surface. Then, each data set was averaged and the resulting averaged Mn-doped  $\text{TiO}_2$  spectra were normalized to the averaged (undoped)  $\text{TiO}_2$  spectrum, with respect to the intensity of the 144 cm<sup>-1</sup> peak.

$\text{N}_2$  adsorption/desorption isotherms at -196 °C were acquired on samples previously outgassed at 200 °C for 2 h (Micromeritics Tristar II) to remove water and other atmospheric contaminants. The sample SSA was calculated according to the BET method; the pore total volume was measured at  $P/P^0 = 0.99$ ; and the pore size distribution was calculated by applying the BJH (Barrett–Joiner–Hallenda) method to isotherm desorption branch.

FESEM micrographs were taken on a ZEISS Supra 40 FESEM instrument (Carl-Zeiss AG, Oberkochen, Germany) equipped with an EDX probe that was used for semi-quantitative determination of the sample chemical composition; typically, on each samples, five spots (ca. 5  $\mu\text{m}^3$  volume) were analyzed and the average Ti, O, and Mn contents were calculated.

DR UV–vis spectra of the powders were recorded on a UV–vis Varian Cary 5000 spectrophotometer equipped with a DR integration sphere in the 200–1000 nm range.

XPS analyses were performed on a Versa Probe II Scanning XPS Microprobe spectrometer (Physical Electronics GmbH). The measurements were carried out with a monochromatized Al  $K\alpha$  source (X-ray spot 100  $\mu\text{m}$ ) at a power of 24.4 W. Wide scans and high-resolution spectra were acquired in fixed analyzer transmission mode with a pass energy of 117.40 and 29.35 eV, respectively. An electron gun was used for charge compensation (1.0 V 20.0  $\mu\text{A}$ ). All the BEs were referenced to the C 1s line at  $284.8 \pm 0.1$  eV for adventitious carbon. Data processing was performed by using the MultiPak software (v. 9.8.0.19).

$\text{H}_2$ -TPR analysis was carried out on a TPD/R/O (temperature-programmed desorption/reduction/oxidation) 1100 ThermoQuest instrument on ca. 50 mg of the sample. In a typical experiment, the powder was kept under constant flow (20 mL min<sup>-1</sup>) of 5%  $\text{H}_2$  in the Ar mixture and heated from room temperature to 800 °C with a ramp of 10 °C min<sup>-1</sup>. The measured  $\text{H}_2$  uptake was then normalized to the sample weight, in order to allow comparison.

$\text{NH}_3$ -TPD (temperature-programmed desorption) analysis was carried out in a quartz bed-fixed reactor connected to a  $\text{NH}_3$  ND-IR (nondispersive infrared) ABB Uras 14 gas analyzer. In each experiment, ca. 200 mg of the sample was pretreated under  $\text{N}_2$  flow (100 mL min<sup>-1</sup>) for 60 min at 500 °C (temperature ramp = 10 °C min<sup>-1</sup>). Then, a mixture of 2000 ppm  $\text{NH}_3$  in He (400 mL min<sup>-1</sup>) was fed into the reactor at 100 °C for the adsorption run, which lasted until the  $\text{NH}_3$  concentration value reached the initial one. The desorption run was performed under  $\text{N}_2$  flow (400 mL min<sup>-1</sup>) first at r.t. to remove the loosely physisorbed fraction and subsequently by increasing the temperature up to 500 °C (temperature ramp = 5 °C min<sup>-1</sup>).

**4.3. Catalytic Activity Measurements.** SCR of  $\text{NO}_x$  was carried out by placing 500 mg of catalyst powder in a fixed bed tubular quartz reactor (inner diameter = 10 mm) under a total feed gas flow rate of 300 N mL min<sup>-1</sup>, which translates to gas hourly space velocity of about 50,000 h<sup>-1</sup>, as values above 30,000 h<sup>-1</sup> are typically used industrially. The gas mixture composition was as follows: 500 ppm NO, 500 ppm  $\text{NH}_3$ , 3%  $\text{O}_2$ , and balance  $\text{N}_2$ .

Catalytic tests were performed under isothermal conditions by increasing  $T$  from 50 to 350 °C with steps of 32 °C and by waiting to reach stable  $T$  and concentrations of the reactive species before each  $T$  increase.

The  $\text{NO}_x$  concentration was analyzed by means of a  $\text{NO}/\text{NO}_2$  UV Limas gas analyzer (ABB SpA) and the  $\text{N}_2\text{O}$  and  $\text{NH}_3$  concentrations by a ND-IR Uras gas analyzer (ABB SpA).

The  $\text{NO}_x$  and  $\text{NH}_3$  conversions and the  $\text{N}_2$  selectivity were calculated from gas concentration according to the following equations

$$\begin{aligned} \text{NO}_x (\text{NO} + \text{NO}_2) \text{ conversion}[\%] \\ = 100 \times \frac{\text{NO}_{x \text{ in}} - \text{NO}_{x \text{ out}}}{\text{NO}_{x \text{ in}}} \end{aligned} \quad (5)$$

$$\text{N}_2 \text{ selectivity}[\%] = 100 \times \frac{\text{N}_2}{\text{N}_2 + \text{N}_2\text{O}} \quad (6)$$

$$\text{Yield}[\%] = \text{N}_2 \text{ selectivity} \times \text{NO}_x \text{ conversion} \quad (7)$$



## ■ ASSOCIATED CONTENT

## ■ Supporting Information

The Supporting Information is available free of charge at <https://pubs.acs.org/doi/10.1021/acsomega.1c03153>.

Raman spectra after subtraction of the undoped TiO<sub>2</sub> spectrum; N<sub>2</sub> adsorption/desorption isotherms at −196 °C; FE-SEM micrographs; and Ti 2p XP spectra (PDF)

## ■ AUTHOR INFORMATION

## Corresponding Author

Serena Esposito – Dipartimento di Scienza Applicata e Tecnologia (DISAT) and INSTM Unit of Torino-Politecnico, Politecnico di Torino, 10129 Torino, Italy; [orcid.org/0000-0001-9159-0541](https://orcid.org/0000-0001-9159-0541); Email: [serena\\_esposito@polito.it](mailto:serena_esposito@polito.it)

## Authors

Barbara Bonelli – Dipartimento di Scienza Applicata e Tecnologia (DISAT) and INSTM Unit of Torino-Politecnico, Politecnico di Torino, 10129 Torino, Italy; [orcid.org/0000-0002-4716-864X](https://orcid.org/0000-0002-4716-864X)

Olimpia Tammaro – Dipartimento di Scienza Applicata e Tecnologia (DISAT) and INSTM Unit of Torino-Politecnico, Politecnico di Torino, 10129 Torino, Italy

Ferenc Martinovic – Dipartimento di Scienza Applicata e Tecnologia (DISAT) and INSTM Unit of Torino-Politecnico, Politecnico di Torino, 10129 Torino, Italy

Roberto Nasi – Dipartimento di Scienza Applicata e Tecnologia (DISAT) and INSTM Unit of Torino-Politecnico, Politecnico di Torino, 10129 Torino, Italy

Gianfranco Dell'Agli – Dipartimento di Ingegneria Civile e Meccanica, Università degli Studi di Cassino e del Lazio Meridionale, 03043 Cassino, Frosinone, Italy

Paola Rivolo – Dipartimento di Scienza Applicata e Tecnologia (DISAT) and INSTM Unit of Torino-Politecnico, Politecnico di Torino, 10129 Torino, Italy; [orcid.org/0000-0003-0672-5793](https://orcid.org/0000-0003-0672-5793)

Fabrizio Giorgis – Dipartimento di Scienza Applicata e Tecnologia (DISAT) and INSTM Unit of Torino-Politecnico, Politecnico di Torino, 10129 Torino, Italy

Nicoletta Ditaranto – Dipartimento di Chimica, Università degli Studi di Bari Aldo Moro, 70125 Bari, Italy

Fabio Alessandro Deorsola – Dipartimento di Scienza Applicata e Tecnologia (DISAT) and INSTM Unit of Torino-Politecnico, Politecnico di Torino, 10129 Torino, Italy

Complete contact information is available at:

<https://pubs.acs.org/doi/10.1021/acsomega.1c03153>

## Notes

The authors declare no competing financial interest.

## ■ REFERENCES

- (1) Konsolakis, M. Recent Advances on Nitrous Oxide (N<sub>2</sub>O) Decomposition over Non-Noble-Metal Oxide Catalysts: Catalytic Performance, Mechanistic Considerations, and Surface Chemistry Aspects. *ACS Catal.* **2015**, *5*, 6397–6421.
- (2) Alunga, K. R.; Ye, Y.-Y.; Li, S.-R.; Wang, D.; Liu, Y.-Q. Catalytic Oxidation of Lignin-Acetoderivatives: A Potential New Recovery Route for Value-Added Aromatic Aldehydes from Acetoderivatives. *Catal. Sci. Technol.* **2015**, *5*, 3746–3753.
- (3) Rosenberg, H. S.; Curran, L. M.; Slack, A. V.; Ando, J.; Oxley, J. H. Post Combustion Methods for Control of NO<sub>x</sub> Emissions. *Prog. Energy Combust. Sci.* **1980**, *6*, 287–302.
- (4) Busca, G.; Lietti, L.; Ramis, G.; Berti, F. Chemical and Mechanistic Aspects of the Selective Catalytic Reduction of NO(x) by Ammonia over Oxide Catalysts: A Review. *Appl. Catal., B* **1998**, *18*, 1–36.
- (5) Gao, F.; Tang, X.; Yi, H.; Zhao, S.; Li, C.; Li, J.; Shi, Y.; Meng, X. A Review on Selective Catalytic Reduction of NO<sub>x</sub> by NH<sub>3</sub> over Mn-Based Catalysts at Low Temperatures: Catalysts, Mechanisms, Kinetics and DFT Calculations. *Catalysts* **2017**, *7*, 199.
- (6) Janssen, F. J. G.; Van Den Kerkhof, F. M. G.; Bosch, H.; Ross, J. R. H. Mechanism of the Reaction of Nitric Oxide, Ammonia, and Oxygen over Vanadia Catalysts. 1. The Role of Oxygen Studied by Way of Isotopic Transients under Dilute Conditions. *J. Phys. Chem.* **1987**, *91*, 5921–5927.
- (7) Wood, S. C. Select the Right NO<sub>x</sub> Control Technology. *Chem. Eng. Prog.* **1994**, *90*, 32.
- (8) Janssens, J. A.; Topsøe, N.-Y.; Topsøe, H.; Chen, Y.; Slabicki, T. Kinetics of Selective Catalytic Reduction of Nitric Oxide by Ammonia over Vanadia/Titania. *J. Catal.* **1996**, *163*, 409–417.
- (9) Ramis, G.; Busca, G.; Bregani, F. On the Effect of Dopants and Additives on the State of Surface Vanadyl Centers of Vanadia-Titania Catalysts. *Catal. Lett.* **1993**, *18*, 299–303.
- (10) Deorsola, F. A.; Andreoli, S.; Armandi, M.; Bonelli, B.; Pirone, R. Unsupported nanostructured Mn oxides obtained by Solution Combustion Synthesis: Textural and surface properties, and catalytic performance in NO<sub>x</sub> SCR at low temperature. *Appl. Catal., A* **2016**, *522*, 120–129.
- (11) Fang, D.; Xie, J.; Hu, H.; Yang, H.; He, F.; Fu, Z. Identification of MnO<sub>x</sub> Species and Mn Valence States in MnO<sub>x</sub>/TiO<sub>2</sub> Catalysts for Low Temperature. *Chem. Eng. J.* **2015**, *271*, 23–30.
- (12) Li, J.; Chang, H.; Ma, L.; Hao, J.; Yang, R. T. Low-Temperature Selective Catalytic Reduction of NO<sub>x</sub> with NH<sub>3</sub> over Metal Oxide and Zeolite Catalysts-A Review. *Catalysis Today*; Elsevier B.V., 2011; Vol. 175; pp 147–156.
- (13) Wu, Z.; Jiang, B.; Liu, Y. Effect of Transition Metals Addition on the Catalyst of Manganese/Titania for Low-Temperature Selective Catalytic Reduction of Nitric Oxide with Ammonia. *Appl. Catal., B* **2008**, *79*, 347–355.
- (14) Xu, G.; Guo, X.; Cheng, X.; Yu, J.; Fang, B. A Review of Mn-Based Catalysts for Low-Temperature NH<sub>3</sub>-SCR: NO: X removal and H<sub>2</sub>O/SO<sub>2</sub> resistance. *Nanoscale* **2021**, *13*, 7052–7080.
- (15) Liu, C.; Shi, J.-W.; Gao, C.; Niu, C. Manganese Oxide-Based Catalysts for Low-Temperature Selective Catalytic Reduction of NO<sub>x</sub> with NH<sub>3</sub>: A Review. *Applied Catalysis A: General*; Elsevier B.V. July, 2016; Vol. 522; pp 54–69.
- (16) Zhu, M.; Lai, J.-K.; Tumuluri, U.; Wu, Z.; Wachs, I. E. Nature of Active Sites and Surface Intermediates during SCR of NO with NH<sub>3</sub> by Supported V<sub>2</sub>O<sub>5</sub>-WO<sub>3</sub>/TiO<sub>2</sub> Catalysts. *J. Am. Chem. Soc.* **2017**, *139*, 15624–15627.
- (17) Yang, J.; Ren, S.; Zhou, Y.; Su, Z.; Yao, L.; Cao, J.; Jiang, L.; Hu, G.; Kong, M.; Yang, J.; Liu, Q. In Situ IR Comparative Study on N<sub>2</sub>O Formation Pathways over Different Valence States Manganese Oxides Catalysts during NH<sub>3</sub>-SCR of NO. *Chem. Eng. J.* **2020**, *397*, 125446.
- (18) Liu, Z.; Chen, C.; Zhao, J.; Yang, L.; Sun, K.; Zeng, L.; Pan, Y.; Liu, Y.; Liu, C. Study on the NO<sub>2</sub> Production Pathways and the Role of NO<sub>2</sub> in Fast Selective Catalytic Reduction DeNO<sub>x</sub> at Low-Temperature over MnO<sub>x</sub>/TiO<sub>2</sub> Catalyst. *Chem. Eng. J.* **2020**, *379*, 122288.
- (19) Ettireddy, P. R.; Ettireddy, N.; Mamedov, S.; Boolchand, P.; Smirniotis, P. G. Surface Characterization Studies of TiO<sub>2</sub> Supported Manganese Oxide Catalysts for Low Temperature SCR of NO with NH<sub>3</sub>. *Appl. Catal., B* **2007**, *76*, 123–134.
- (20) Smirniotis, P. G.; Sreekanth, P. M.; Peña, D. A.; Jenkins, R. G. Manganese Oxide Catalysts Supported on TiO<sub>2</sub>, Al<sub>2</sub>O<sub>3</sub>, and SiO<sub>2</sub>: A Comparison for Low-Temperature SCR of NO with NH<sub>3</sub>. *Ind. Eng. Chem. Res.* **2006**, *45*, 6436–6443.
- (21) Sultana, A.; Sasaki, M.; Hamada, H. Influence of Support on the Activity of Mn Supported Catalysts for SCR of NO with Ammonia. *Catal. Today* **2012**, *185*, 284–289.



- (22) Putluru, S. S. R.; Schill, L.; Jensen, A. D.; Siret, B.; Tabaries, F.; Fehrmann, R. Mn/TiO<sub>2</sub> and Mn-Fe/TiO<sub>2</sub> Catalysts Synthesized by Deposition Precipitation-Promising for Selective Catalytic Reduction of NO with NH<sub>3</sub> at Low Temperatures. *Appl. Catal., B* **2015**, *165*, 628–635.
- (23) Rossetti, I.; Bonelli, B.; Ramis, G.; Bahadori, E.; Nasi, R.; Aronne, A.; Esposito, S. New Insights into the Role of the Synthesis Procedure on the Performance of Co-Based Catalysts for Ethanol Steam Reforming. *Top. Catal.* **2018**, *61*, 1734–1745.
- (24) Esposito, S.; Setaro, A.; Maddalena, P.; Aronne, A.; Pernice, P.; Laracca, M. Synthesis of Cobalt Doped Silica Thin Film for Low Temperature Optical Gas Sensor. *J. Sol-Gel Sci. Technol.* **2011**, *60*, 388–394.
- (25) Minieri, L.; Esposito, S.; Russo, V.; Bonelli, B.; Di Serio, M.; Silvestri, B.; Vergara, A.; Aronne, A. A Sol–Gel Ruthenium–Niobium–Silicon Mixed-Oxide Bifunctional Catalyst for the Hydrogenation of Levulinic Acid in the Aqueous Phase. *ChemCatChem* **2017**, *9*, 1476–1486.
- (26) Bagnasco, G.; Cammarano, C.; Turco, M.; Esposito, S.; Aronne, A.; Pernice, P. TPR/TPO Characterization of Cobalt-Silicon Mixed Oxide Nanocomposites Prepared by Sol-Gel. *Thermochim. Acta* **2008**, *471*, 51–54.
- (27) Esposito, S.; Turco, M.; Bagnasco, G.; Cammarano, C.; Pernice, P. New Insight into the Preparation of Copper/Zirconia Catalysts by Sol-Gel Method. *Appl. Catal., A* **2011**, *403*, 128–135.
- (28) Prasad, S.; Kumar, V.; Kirubanandam, S.; Barhoum, A. Engineered Nanomaterials: Nanofabrication and Surface Functionalization. *Emerging Applications of Nanoparticles and Architectural Nanostructures: Current Prospects and Future Trends*; Elsevier Inc., 2018; pp 305–340.
- (29) Su, C.; Hong, B.-Y.; Tseng, C.-M. Sol–Gel Preparation and Photocatalysis of Titanium Dioxide. *Catal. Today* **2004**, *96*, 119–126.
- (30) Dell'Agli, G.; Esposito, S.; Mascolo, G.; Mascolo, M. C.; Pagliuca, C. Films by Slurry Coating of Nanometric YSZ (8 Mol% Y<sub>2</sub>O<sub>3</sub>) Powders Synthesized by Low-Temperature Hydrothermal Treatment. *J. Eur. Ceram. Soc.* **2005**, *25*, 2017–2021.
- (31) Wu, Z.; Jiang, B.; Liu, Y.; Zhao, W.; Guan, B. Experimental Study on a Low-Temperature SCR Catalyst Based on MnO<sub>x</sub>/TiO<sub>2</sub> Prepared by Sol-Gel Method. *J. Hazard. Mater.* **2007**, *145*, 488–494.
- (32) Kim, Y. J.; Kwon, H. J.; Nam, I.-S.; Choung, J. W.; Kil, J. K.; Kim, H.-J.; Cha, M.-S.; Yeo, G. K. High DeNO<sub>x</sub> Performance of Mn/TiO<sub>2</sub> Catalyst by NH<sub>3</sub>. *Catalysis Today*; Elsevier, 2010; Vol. 151; pp 244–250.
- (33) Esposito, S. "Traditional" Sol-Gel Chemistry as a Powerful Tool for the Preparation of Supported Metal and Metal Oxide Catalysts. *Materials (Basel)* **2019**, *12*, 668.
- (34) Hanaor, D. A. H.; Sorrell, C. C. Review of the Anatase to Rutile Phase Transformation. *J. Mater. Sci.* **2011**, *46*, 855–874.
- (35) Shannon, R. D. Revised Effective Ionic Radii and Systematic Studies of Interatomic Distances in Halides and Chalcogenides. *Acta Crystallogr. Sect. A* **1976**, *32*, 751–767.
- (36) Tompsett, G. A.; Bowmaker, G. A.; Cooney, R. P.; Metson, J. B.; Rodgers, K. A.; Seakins, J. M. The Raman Spectrum of Brookite, TiO<sub>2</sub> (Pbc<sub>2</sub>, Z = 8). *J. Raman Spectrosc.* **1995**, *26*, 57–62.
- (37) Pérez-Larios, A.; Hernández-Gordillo, A.; Morales-Mendoza, G.; Lartundo-Rojas, L.; Mantilla, Á.; Gómez, R. Enhancing the H<sub>2</sub> Evolution from Water-Methanol Solution Using Mn<sup>2+</sup>-Mn<sup>3+</sup>-Mn<sup>4+</sup> Redox Species of Mn-Doped TiO<sub>2</sub> Sol-Gel Photocatalysts. *Catalysis Today*; Elsevier B.V., 2016; Vol. 266; pp 9–16.
- (38) Sultana, A.; Sasaki, M.; Hamada, H. Influence of Support on the Activity of Mn Supported Catalysts for SCR of NO with Ammonia. *Catalysis Today*; Elsevier, 2012; Vol. 185; pp 284–289.
- (39) Xue, M.; Huang, L.; Wang, J.-Q.; Wang, Y.; Gao, L.; Zhu, J.-h.; Zou, Z.-G. The Direct Synthesis of Mesoporous Structured MnO<sub>2</sub>/TiO<sub>2</sub> Nanocomposite: A Novel Visible-Light Active Photocatalyst with Large Pore Size. *Nanotechnology* **2008**, *19*, 185604.
- (40) Hsu, Y.-K.; Chen, Y.-C.; Lin, Y.-G.; Chen, L.-C.; Chen, K.-H. Birnessite-Type Manganese Oxides Nanosheets with Hole Acceptor Assisted Photoelectrochemical Activity in Response to Visible Light. *J. Mater. Chem.* **2012**, *22*, 2733–2739.
- (41) Ristić, A.; Mazaj, M.; Arčon, I.; Daneu, N.; Zabukovec Logar, N.; Gläser, R.; Tušar, N. N. New Insights into Manganese Local Environment in MnS-1 Nanocrystals. *Cryst. Growth Des.* **2019**, *19*, 3130–3138.
- (42) Deng, Q. R.; Xia, X. H.; Guo, M. L.; Gao, Y.; Shao, G. Mn-Doped TiO<sub>2</sub> Nanopowders with Remarkable Visible Light Photocatalytic Activity. *Mater. Lett.* **2011**, *65*, 2051–2054.
- (43) Shao, G. Red Shift in Manganese- And Iron-Doped TiO<sub>2</sub>: A DFT + u Analysis. *J. Phys. Chem. C* **2009**, *113*, 6800–6808.
- (44) Esposito, S.; Ditaranto, N.; Dell'Agli, G.; Nasi, R.; Rivolo, P.; Bonelli, B. Effective Inclusion of Sizable Amounts of Mo within TiO<sub>2</sub> Nanoparticles Can Be Obtained by Reverse Micelle Sol-Gel Synthesis. *ACS Omega* **2021**, *6*, 5379.
- (45) Nasi, R.; Esposito, S.; Freyria, F.; Armandi, M.; Gadhi, T.; Hernandez, S.; Rivolo, P.; Ditaranto, N.; Bonelli, B. Application of Reverse Micelle Sol-Gel Synthesis for Bulk Doping and Heteroatoms Surface Enrichment in Mo-Doped TiO<sub>2</sub> Nanoparticles. *Materials (Basel)* **2019**, *12*, 937.
- (46) Biesinger, M. C.; Payne, B. P.; Grosvenor, A. P.; Lau, L. W. M.; Gerson, A. R.; Smart, R. S. C. Resolving Surface Chemical States in XPS Analysis of First Row Transition Metals, Oxides and Hydroxides: Cr, Mn, Fe, Co and Ni. *Appl. Surf. Sci.* **2011**, *257*, 2717–2730.
- (47) Oku, M.; Hirokawa, K.; Ikeda, S. X-Ray Photoelectron Spectroscopy of Manganese-Oxygen Systems. *J. Electron Spectrosc. Relat. Phenom.* **1975**, *7*, 465–473.
- (48) Banerjee, D.; Nesbitt, H. W. XPS Study of Dissolution of Birnessite by Humate with Constraints on Reaction Mechanism. *Geochim. Cosmochim. Acta* **2001**, *65*, 1703–1714.
- (49) Nesbitt, H. W.; Banerjee, D. Interpretation of XPS Mn(2p) Spectra of Mn Oxyhydroxides and Constraints on the Mechanism of MnO<sub>2</sub> Precipitation. *Am. Mineral.* **1998**, *83*, 305–315.
- (50) Banerjee, D.; Nesbitt, H. W. Oxidation of Aqueous Cr(III) at Birnessite Surfaces: Constraints on Reaction Mechanism. *Geochim. Cosmochim. Acta* **1999**, *63*, 1671–1687.
- (51) Wang, L.; Huang, B.; Su, Y.; Zhou, G.; Wang, K.; Luo, H.; Ye, D. Manganese Oxides Supported on Multi-Walled Carbon Nanotubes for Selective Catalytic Reduction of NO with NH<sub>3</sub>: Catalytic Activity and Characterization. *Chem. Eng. J.* **2012**, *192*, 232–241.
- (52) Tang, X.; Li, J.; Sun, L.; Hao, J. Origination of N<sub>2</sub>O from NO reduction by NH<sub>3</sub> over β-MnO<sub>2</sub> and α-Mn<sub>2</sub>O<sub>3</sub>. *Appl. Catal., B* **2010**, *99*, 156–162.
- (53) Han, Y.-F.; Chen, F.; Zhong, Z.; Ramesh, K.; Chen, L.; Widjaja, E. Controlled Synthesis, Characterization, and Catalytic Properties of Mn<sub>2</sub>O<sub>3</sub> and Mn<sub>3</sub>O<sub>4</sub> Nanoparticles Supported on Mesoporous Silica SBA-15. *J. Phys. Chem. B* **2006**, *110*, 24450–24456.
- (54) Xiong, L.-B.; Li, J.-L.; Yang, B.; Yu, Y. Ti<sup>3+</sup> in the Surface of Titanium Dioxide: Generation, Properties and Photocatalytic Application. *Journal of Nanomaterials* **2012**, *2012*, 9.
- (55) Xaba, B. M.; De Villiers, J. P. R. Sintering Behavior of TiO<sub>2</sub>-Supported Model Cobalt Fischer-Tropsch Catalysts under H<sub>2</sub> Reducing Conditions and Elevated Temperature. *Ind. Eng. Chem. Res.* **2016**, *55*, 9397–9407.
- (56) Xu, Q.; Fang, Z.; Chen, Y.; Guo, Y.; Guo, Y.; Wang, L.; Wang, Y.; Zhang, J.; Zhan, W. Titania-Samarium-Manganese Composite Oxide for the Low-Temperature Selective Catalytic Reduction of NO with NH<sub>3</sub>. *Environ. Sci. Technol.* **2020**, *54*, 2530–2538.
- (57) Petrik, I. S.; Krylova, G. V.; Kelyp, O. O.; Lutsenko, L. V.; Smirnova, N. P.; Oleksenko, L. P. XPS and TPR Study of Sol-Gel Derived M/TiO<sub>2</sub> Powders (M=Co, Cu, Mn, Ni). *Him. Fiz. ta Tehnol. Poverhni* **2015**, *6*, 179–189.
- (58) Xiong, M.; Gao, Z.; Zhao, P.; Wang, G.; Yan, W.; Xing, S.; Wang, P.; Ma, J.; Jiang, Z.; Liu, X.; Ma, J.; Xu, J.; Qin, Y. In Situ Tuning of Electronic Structure of Catalysts Using Controllable Hydrogen Spillover for Enhanced Selectivity. *Nat. Commun.* **2020**, *11*, 1–10.
- (59) Esposito, S.; Silvestri, B.; Russo, V.; Bonelli, B.; Manzoli, M.; Deorsola, F. A.; Vergara, A.; Aronne, A.; Di Serio, M. Self-Activating

Catalyst for Glucose Hydrogenation in the Aqueous Phase under Mild Conditions. *ACS Catal.* **2019**, *9*, 3426–3436.

(60) Esposito, S.; Dell'Agli, G.; Marocco, A.; Bonelli, B.; Allia, P.; Tiberto, P.; Barrera, G.; Manzoli, M.; Arletti, R.; Pansini, M. Magnetic Metal-Ceramic Nanocomposites Obtained from Cation-Exchanged Zeolite by Heat Treatment in Reducing Atmosphere. *Microporous Mesoporous Mater.* **2018**, *268*, 131–143.

(61) Esposito, S.; Turco, M.; Bagnasco, G.; Cammarano, C.; Pernice, P.; Aronne, A. Highly Dispersed Sol-Gel Synthesized Cu-ZrO<sub>2</sub> Materials as Catalysts for Oxidative Steam Reforming of Methanol. *Appl. Catal., A* **2010**, *372*, 48–57.

(62) Shen, B.; Liu, T.; Zhao, N.; Yang, X.; Deng, L. Iron-Doped Mn-Ce/TiO<sub>2</sub> Catalyst for Low Temperature Selective Catalytic Reduction of NO with NH<sub>3</sub>. *J. Environ. Sci.* **2010**, *22*, 1447–1454.

(63) Zhan, S.; Zhu, D.; Qiu, M.; Yu, H.; Li, Y. Highly Efficient Removal of NO with Ordered Mesoporous Manganese Oxide at Low Temperature. *RSC Adv.* **2015**, *5*, 29353–29361.

(64) Kapteijn, F.; Vanlangeveld, A. D.; Moulijn, J. A.; Andreini, A.; Vuurman, M. A.; Turek, A. M.; Jehng, J. M.; Wachs, I. E. Alumina-Supported Manganese Oxide Catalysts. *J. Catal.* **1994**, *150*, 94–104.

(65) Ettireddy, P. R.; Ettireddy, N.; Boningari, T.; Pardemann, R.; Smirniotis, P. G. Investigation of the selective catalytic reduction of nitric oxide with ammonia over Mn/TiO<sub>2</sub> catalysts through transient isotopic labeling and in situ FT-IR studies. *J. Catal.* **2012**, *292*, 53–63.

(66) Mihai, O.; Widyastuti, C. R.; Kumar, A.; Li, J.; Joshi, S. Y.; Kamasamudram, K.; Currier, N. W.; Yezerets, A.; Olsson, L. The Effect of NO<sub>2</sub>/NO<sub>x</sub> Feed Ratio on the NH<sub>3</sub>-SCR System Over Cu-Zeolites with Varying Copper Loading. *Catal. Lett.* **2014**, *144*, 70–80.

(67) Xie, S.; Li, L.; Jin, L.; Wu, Y.; Liu, H.; Qin, Q.; Wei, X.; Liu, J.; Dong, L.; Li, B. Low Temperature High Activity of M (M = Ce, Fe, Co, Ni) Doped M-Mn/TiO<sub>2</sub> Catalysts for NH<sub>3</sub>-SCR and in Situ DRIFTS for Investigating the Reaction Mechanism. *Appl. Surf. Sci.* **2020**, *515*, 146014.

(68) Huang, J.; Huang, H.; Liu, L.; Jiang, H. Revisit the Effect of Manganese Oxidation State on Activity in Low-Temperature NO-SCR. *Mol. Catal.* **2018**, *446*, 49–57.

(69) Andreoli, S.; Deorsola, F. A.; Galletti, C.; Pirone, R. Nanostructured MnO catalysts for low-temperature NO SCR. *Chem. Eng. J.* **2015**, *278*, 174–182.

(70) Lou, X.; Liu, P.; Li, J.; Li, Z.; He, K. Effects of Calcination Temperature on Mn Species and Catalytic Activities of Mn/ZSM-5 Catalyst for Selective Catalytic Reduction of NO with Ammonia. *Appl. Surf. Sci.* **2014**, *307*, 382–387.

(71) Eastoe, J.; Hollamby, M. J.; Hudson, L. Recent Advances in Nanoparticle Synthesis with Reversed Micelles. *Adv. Colloid Interface Sci.* **2006**, *128–130*, 5–15.

(72) Lutterotti, L.; Bortolotti, M.; Ischia, G.; Lonardelli, I.; Wenk, H.-R. Rietveld Texture Analysis from Diffraction Images. *Zeitschrift für Kristallographie, Supplement*; R. Oldenbourg Verlag GmbH, 2007; Vol. 2007, pp 125–130.